

3D Tomographic Reconstruction of an Absorptive Perturbation with Diffuse Photon Density Waves

[Accepted JOSA]

Matthew Braunstein and Robert Y. Levine

Spectral Sciences, Inc., 99 S. Bedford St., Suite 7, Burlington, MA 01803-5169

ABSTRACT

A 3D tomographic reconstruction algorithm for an absorptive perturbation in tissue is derived. The input consists of multiple 2D projected views of tissue that is back-illuminated with diffuse photon density waves (DPDWs). The algorithm is based on a generalization of the Projection-Slice Theorem and consists of depth estimation, image deconvolution, filtering, and backprojection. The formalism provides estimates of the number of views necessary to achieve a given spatial resolution in the reconstruction. The algorithm is demonstrated with data simulated to mimic the absorption of a contrast agent in human tissue. The effects of noise and uncertainties in the depth estimate are explored.

1. INTRODUCTION

The theory of tomographic reconstruction, taking as input multiple projections of an object, is at the foundation of diverse medical applications such as Computer Aided Tomography¹, Magnetic Resonance Imaging, Emission Computed Tomography, and Intensity Modulated Radiation Therapy². In this paper tomographic reconstruction of tissue anomalies from diffuse photon density wave (DPDW) images is considered.^{3,4} Tomographic reconstruction of absorption and scattering parameters from DPDW images is defined as a 3D reconstruction from multiple 2D projections of back-illuminated tissue. This is distinct from the more common inversion of the diffusion equation to match point-source/detector boundary conditions⁵⁻⁹. In the latter case, the term ‘tomography’ often refers to the reconstruction of objects in two dimensional slices through the tissue. DPDW tissue imaging, utilizing non-ionizing near-IR photons, may provide unique information about the presence of cancerous tissue and *in-vivo* tissue functioning. It has been an area of intense research in recent years¹⁰.

Near-IR photons in the range ($0.7\mu - 1.2\mu$) penetrate deep into tissue but are highly scattered so that a projected image appears highly blurred¹¹⁻¹³. The incorporation of scattering effects in the model for photon propagation, with the goal of defining an inversion algorithm from projected images or detector array responses, has appeared in a number of papers^{5-9,14-19}. The tomographic techniques generally involve the definition of image filters or scattering kernels to compensate for the photon migration through homogeneous tissues¹⁴⁻¹⁷. The procedure derived in this paper is in this category of DPDW image reconstruction. It is shown that for a small absorptive perturbation in tissue, such as caused by the accumulation of a contrast agent in a tumor, the photon diffusion equation and boundary conditions lead to a generalized 3D tomographic reconstruction algorithm

for the perturbation involving depth estimation, image deconvolution, and backprojection. The procedure is based on a generalization of the Projection-Slice Theorem²⁰ which relates the Fourier transform of the projection to a slice of the 3D tissue Fourier transform times an extra depth-dependent term. This extends an analysis in Ref.(19) to the case of multiple projections. The reconstruction is necessarily three dimensional because of the migration of photons out of the plane of entry before and after interaction with the absorptive perturbation. Alternative reconstruction schemes include the fitting of detector responses to parameterized solutions of the diffusion equation²¹⁻²³. However, without the imposition of the projection geometry in the data, the conditioning of the inversion is less certain. The algorithm presented here could provide a computationally inexpensive initial solution to improve the conditioning of these techniques.

Scattering and absorption artifacts, such as bone or blood vessels, may be poorly modeled using the homogeneous tissue DPDW diffusion equation. For the imaging of tumors, the problem of artifacts is partially overcome by the use of contrast agents. There is evidence that, possibly due to immature, leaky vasculature²⁴, an intravenous contrast agent persists at the tumor site^{25,26}. The imaging of early-stage tumor vasculature may be important in determining the likelihood of metastases^{24,27}. Internal bleeding detection is another application in which the persistent accumulation of a contrast agent could be imaged²⁸. In recent years it has been shown that multi-spectral imaging could be used to isolate accumulations in tissue of a contrast agent with a strong near-IR absorption edge²⁹⁻³¹. For example, a clinically feasible compound with negligible medical complications, Indocyanine Green (ICG), has been studied for these applications³². Alternatively, near-IR imaging before and after the introduction of the agent could isolate the drug in a tumor.

In this paper a unified 3D tomographic reconstruction algorithm for absorptive perturbations, such as arising from an accumulated contrast agent, is derived. The 3D geometry is suggested by photon migration and the feasibility of measuring 2D transilluminated images on the tissue surface with a CCD camera^{29,30}. The tomographic geometry and boundary conditions assume a flat image plane that can be implemented through the use of a bolus matched to the diffusion equation parameters of the tissue³³. We show that the difference of camera images between absorption and transmission wavelengths approximates the x-ray transform of the 3D function defining the agent attenuation constant in tissue. This is the basis of the reconstruction algorithm.

The paper will proceed as follows. Section 2 contains the derivation of the projection image from bi-spectral measurements of a diffuse photon density wave. The treatment, which is similar to Ref.(19), leads to a generalized 3D Projection-Slice Theorem²⁰ as the basis for image reconstruction from multiple views. Inversion to the 3D perturbative attenuation function requires depth estimation and image deconvolution, both of which are discussed in Section 3. This is combined with a known 3D x-ray transform inversion algorithm²⁰ in Section 4. Section 5 presents a demonstration calculation of the algorithm using simulated data designed to mimic the absorption of a contrast agent in tissue. Section 6 gives conclusions. Appendices A and B contain derivations of a sufficient number and optimum orientation of projected images for the 3D reconstruction, respectively.

2. TOMOGRAPHIC DPDW MODEL

In this section the formalism in Ref.(19) is reviewed and extended to multiple views for 3D tomographic reconstruction of a perturbative absorbing agent. As appearing in the diffusion equation^{3,4}, photon propagation in tissue is characterized by absorption and (reduced) scattering constants, μ_a and μ'_s , diffusion constant $D_0 = v/(3\mu'_s)$ for photon velocity v , and the DPDW

complex wavenumber $k_0 = \sqrt{(-\mu_a \nu + i\omega) / D_0}$ for DPDW modulation frequency ω . For simplicity consider the dc limit $\omega \rightarrow 0$ and substitute for D_0 to define a DPDW attenuation constant $\kappa_0 = \sqrt{3\mu_a \mu'_s}$. Typical values of $\mu_a = .02 \text{cm}^{-1}$ and $\mu'_s = 8.0 \text{cm}^{-1}$ in tissue correspond to an attenuation of $\kappa_0 = 0.69 \text{cm}^{-1}$.

The geometry of interest, with sideview shown in Fig. 1, is of a contrast agent attenuation function $\delta\mu_a(\vec{r})$, proportional to the agent density, centered at $z = z_t$ between the source ($z = 0$) and detector ($z = z_d$) planes. An input DPDW $U_0(\vec{r}, \vec{r}_s)$ in the medium is perturbed by the contrast agent to yield a detector plane image difference between transmission and absorption bands,

$$U_{it} = U(\lambda_{trans}) - U(\lambda_{abs}), \quad (1)$$

given by¹⁹

$$U_{it}(\vec{r}_d, \vec{r}_s) = \frac{\nu}{D_0} \int \delta\mu_a(\vec{r}) U_0(\vec{r}, \vec{r}_s) G(\vec{r}_d - \vec{r}) d\vec{r}, \quad (2)$$

where \vec{r}_s and \vec{r}_d are vectors to the source and detector planes, respectively, and where G is the diffusion equation Green's function for a homogeneous medium given in Ref.(19),

$$G(\vec{r}) = \frac{1}{8\pi^2} \int \frac{dpdq}{\mu(p, q)} \exp[ipx + iqy - \mu(p, q)z], \quad (3)$$

with

$$\mu(p, q) = \sqrt{\kappa_0^2 + p^2 + q^2}, \quad (4)$$

and where (p, q) defines the wavenumber coordinate in the image Fourier plane. The expression in Eq.(3), known as the Weyl expansion, is appropriate for an infinite homogeneous tissue space.

Uniform illumination of the tissue surface for an infinite half-plane in Fig. 1 corresponds to a z -dependent photon density given by,

$$V_0(z) = A_1 \exp(-\kappa_0 z) + A_2 \exp(-\mu_t z), \quad (5)$$

where $\mu_t = \mu_a + \mu_s$ ^(5,34). From the parameters defined above, the value $\mu_t = 8.02 \text{ cm}^{-1}$ suggests that an absorptive perturbation of depth greater than $\approx 1.0 \text{ mm}$ has an incident photon density $V_0(z) \cong A_1 e^{-\kappa_0 z}$ corresponding to the infinite medium. The resulting difference of output photon densities is given by

$$U_{1t}(\vec{r}_d) = \frac{v}{D_0} \int \delta\mu_a(\vec{r}) G(\vec{r}_d - \vec{r}) V_0(z) d\vec{r}. \quad (6)$$

Substitution of Eq.(3) into Eq.(6) and rearrangement of integrals results in the expression

$$U_{1t}(\vec{r}_d) = \frac{v}{8\pi^2 D_0} \int \frac{dpdq}{\mu(p,q)} \exp(ipx_d + iqy_d) \int dz V_0(z) \exp(-\mu(p,q)(z_d - z)) \int dx dy \delta\mu_a(x,y,z) \exp(-ipx - iqy). \quad (7)$$

Taking the Fourier transform of U_{1t} with respect to (x_d, y_d) in the image plane $\vec{r}_d = (x_d, y_d, z_d)$ yields

$$\tilde{U}_{1t}(p,q,z_d) = \frac{v}{8\pi^2 D_0} \frac{1}{\mu(p,q)} \int dz V_0(z) \exp(-\mu(p,q)(z_d - z)) \delta\tilde{\mu}_a(p,q,z), \quad (8)$$

where $\delta\tilde{\mu}_a(p,q,z)$ is the two-dimensional Fourier transform of $\mu_a(x,y,z)$. In order to isolate the function $\delta\tilde{\mu}_a(p,q,z)$ in a projection integral, it is necessary to remove the multiplying factors from the integrand in Eq.(8). For example, it is assumed that the quantity $\exp(-\mu(p,q)(z_d - z))$ is relatively

slowly varying over a perturbation centered at z_0 and extending over a range $2l$, ($z_0 \pm l$),

$$\frac{|\exp(-\mu(p, q)(z_d - z_0 - l)) - \exp(-\mu(p, q)(z_d - z_0 + l))|}{\exp(-\mu(p, q)(z_d - z_0))} = |\exp(\mu(p, q)l) - \exp(-\mu(p, q)l)| \ll 1. \quad (9)$$

This condition requires $\mu(p, q)l \ll 1$ which from Eq.(4) yields

$$l \ll \frac{1}{\sqrt{\kappa_0^2 + p^2 + q^2}} < \frac{1}{\kappa_0}. \quad (10)$$

Therefore, the object must be small compared to the inverse attenuation $\kappa_0^{-1} \cong 1.4 \text{ cm}$. The expression in Eq.(10) also constrains the reconstructed spatial frequencies in $\delta\tilde{\mu}_a(p, q, z)$ to satisfy

$$(p^2 + q^2) \ll \left(\frac{1}{l^2} - \kappa_0^2 \right), \quad (11)$$

indicating that the reconstructed transverse spatial frequencies are somewhat less (by κ_0^2) than the inverse of the z -extent of the object. Equations (10) and (11) suggest that it is difficult to reconstruct features of the perturbation much more resolved than the object size. For uniform illumination of absorptive perturbations at depths greater than 1 mm , the attenuation length of $V_0(z)$ in Eq.(5) is expected of order κ_0^{-1} so that the condition on l is less constrained than in Eq.(10). These assumptions allow the localization of the integrand factors of $\delta\tilde{\mu}_a$ in Eq.(8) to $z = z_t$ with the result,

$$\tilde{U}_{1t}(p, q, z_d) = \frac{vV_0(z_t) \exp(-\mu(p, q)(z_d - z_t))}{8\pi^2 D_0 \mu(p, q)} \delta\tilde{\mu}_a(p, q, 0), \quad (12)$$

where $\delta\tilde{\mu}_a(p, q, 0)$ is the $k_z=0$ slice of the 3D Fourier transform of $\delta\mu_a(x, y, z)$. Note that \tilde{U}_{1t} is the Fourier transform of the projection along the z -axis, which is generalized for multiple views to a look direction $\hat{\theta}$.

The expression in Eq.(12), which is a key result in this paper, is a generalization of the well-known Projection-Slice Theorem²⁰ relating the Fourier transforms of projections and reconstructed objects. In this case the 2D Fourier transformed projection, \tilde{U}_{1r} , is proportional to the corresponding slice through the 3D Fourier transform of $\delta\mu_a$. In addition to $\delta\tilde{\mu}_a$, there is a depth and spatial frequency-dependent factor

$$\tilde{D}_\theta = \frac{v}{8\pi^2 D_0} \frac{V_0(z_t) \exp(-\mu(p, q) \Delta z)}{\mu(p, q)}, \quad (13)$$

where $\Delta z = (z_d - z_t)$. Aside from this factor, which requires special processing discussed in Section 3, the inversion of Eq.(12) for multiple views is a known generalization of the backprojection-of-filtered-projections algorithm used in CT reconstruction^{1,20}. This algorithm will be summarized in Section 4.

3. POINT SOURCE SOLUTION AND DEPTH ESTIMATE

In order to invert Eq.(6) for $\delta\mu_a$ from multiple views it is necessary to remove the depth dependent factor \tilde{D}_θ (in Eq.(13)), which implies knowledge of the depth of the perturbation. We now show that the depth can be estimated by relating the difference image at each angle to the first-order solution to a point perturbation, ($\delta\mu_a(x) = s\delta(x)$). Assuming that the perturbation is a point to first order, the output photon density is obtained from the inverse Fourier transform of Eq.(12) as

$$U_{1r}(\vec{r}_d) = V_{10} \int \frac{\exp[-\kappa_0 \Delta z \sqrt{1 + (p^2 + q^2)/\kappa_0^2}]}{\sqrt{1 + (p^2 + q^2)/\kappa_0^2}} \exp(i(x_d p + y_d q)) dp dq, \quad (14)$$

where $V_{10} = v s V_0(z_t)/(8\pi^2 D_0)$. Evaluation of Eq.(14) yields the point source solution for the difference of output photon densities given by

$$U_{1_t}(x_d, y_d) = \frac{2\pi V_{10} \kappa_0 \exp[-\kappa_0 \sqrt{\Delta z^2 + r^2}]}{\sqrt{\Delta z^2 + r^2}}, \quad (15)$$

where $r = \sqrt{x_d^2 + y_d^2}$ on the detector plane. Note that, although there is depth (z_t) dependence in the factor V_{10} , the normalized *width* of the blurred spot described in Eq.(15) determines Δz .

The initial step in a robust depth estimation algorithm to determine Δz is to identify the detector plane location of maximum fluence at the origin. Then the image plane density is integrated over a disk of radius R centered on this point to obtain the function,

$$A(R) = \int_0^R 2\pi r U_{1_t}(r) dr \quad (16)$$

which upon substitution of Eq.(15) yields,

$$A(R) = (2\pi)^2 V_{10} [\exp(-\kappa_0 \Delta z) - \exp(-\kappa_0 \sqrt{\Delta z^2 + R^2})]. \quad (17)$$

Subtraction and normalization by the total image intensity results in an expression independent of V_{10} ,

$$\psi(R) = \ln \left[\frac{A(\infty) - A(R)}{A(\infty)} \right] = \kappa_0 [\Delta z - \sqrt{\Delta z^2 + R^2}]. \quad (18)$$

The solution of Eq.(18) for Δz yields a depth estimate $\Delta \hat{z}$ as a function of R

$$\Delta \hat{z}(R) = \left[\frac{(\psi / \kappa_0)^2 - R^2}{2(\psi / \kappa_0)} \right], \quad (19)$$

which, in the perturbative limit for a point density, should be constant as a function of R . Therefore, the average of depth estimates from multiple disk radii defines an overall depth. This method of

depth estimation was applied recently using *in vitro* ICG injections in back-illuminated tissue from bi-spectral CCD camera images on the surface^{29,30}.

4. DPDW-BASED 3D RECONSTRUCTION ALGORITHM

The results in Sections 2 and 3 can be combined with the x-ray transform inversion algorithm to define a unified 3D reconstruction algorithm for the perturbative attenuation. Assume that a series of 2D views of contrast agent accumulation is obtained in the spherical geometry of Fig.2. The 2D image plane represents the focussed CCD camera face. It is assumed that images are recorded with uniform illumination of the opposing tissue surface.

The procedure in Section 3 is applied for each $\hat{\theta}$ in Fig.2 to obtain a $\hat{\theta}$ -dependent depth estimate $\Delta\hat{z}(\hat{\theta})$, and associated length $z_t(\hat{\theta})$, from Eq.(19). A point source deconvolution, equivalent to division of $\tilde{U}_{1_t}(p, q)$ by $\tilde{D}_{\hat{\theta}}$ with $\Delta z = \Delta\hat{z}(\hat{\theta})$, is applied to $U_{1_t}(\vec{r}_d)$. Note that this includes division by $V_{1_0}(z_t)$, where $z_t(\hat{\theta})$ is determined by the depth estimate. As seen from the 3D Projection-Slice Theorem and Eq.(12), the image at $\hat{\theta}$ after deconvolution, denoted $V(\hat{\theta}, \vec{r}_d)$, represents the x-ray transform of the attenuation function $\delta\mu_a(\vec{r})$. This transform is defined by the projection of $\delta\mu_a(\vec{r})$ along rays orthogonal to the image plane

$$V(\hat{\theta}, \vec{r}_d) = \int_{-\infty}^{\infty} \delta\mu_a((R_0 - t)\hat{\theta} + \vec{r}_d) dt, \quad (20)$$

where R_0 is the radius of the imaging sphere⁸. The radius R_0 is defined by the common center of 3D rotation for the imaging planes.

The inversion of the function $V(\hat{\theta}, \vec{r}_d)$ to $\delta\mu_a(\vec{r})$ is a generalization of the backprojection-of-filtered-projections algorithm in CT given by^{1,20}

$$\delta\mu_a(\vec{r}) = P^\# [J \otimes V], \quad (21)$$

where $P^\#$ is the dual x-ray transform (a 3D backprojection) defined as

$$P^\# [f(\hat{\theta}, \vec{r}_d)](\vec{r}) = \int f[\hat{\theta}, (\vec{r} \cdot \hat{\theta}_1)\hat{\theta}_1 + (\vec{r} \cdot \hat{\theta}_2)\hat{\theta}_2] d\hat{\theta}, \quad (22)$$

where $(\hat{\theta}_1, \hat{\theta}_2, \hat{\theta})$ (see Fig.2) forms an orthogonal triad of vectors for every beam direction $\hat{\theta}$. The 2D filter J , a generalization of the corresponding profile filter in CT reconstruction, is given by

$$\tilde{J}f(\hat{\theta}, \vec{k}) = |\vec{k}| \tilde{f}(\hat{\theta}, \vec{k}), \quad (23)$$

where \tilde{f} denotes the Fourier transform, and \vec{k} is the 2D spatial frequency vector in the $\hat{\theta}$ -image domain. The unified reconstruction algorithm is then given by

$$\delta\hat{\mu}_a = P^\# [J \otimes D_\theta^{-1} \otimes U_{l_r}], \quad (24)$$

where $P^\#$ is the dual x-ray transform in Eq.(22), J is the image filter in Eq.(23), $\{D_\theta^{-1}\}$ are the depth dependent point source deconvolution filters, and $\{U_{l_r}(\hat{\theta}, \vec{r}_d)\}$ are the bi-spectral difference images at view angles $\{\hat{\theta}\}$. We note that this result, deconvolution and filtering followed by backprojection, is similar to algorithms pursued elsewhere.^{16,17} But the filtering described here is more general and allows for fine adjustment to be made to resolve perturbations at different depths.

In addition to suggesting a reconstruction algorithm, the tomographic formulation of near-IR imaging is useful for estimates of the required number of views and optimum look directions³⁵. For example, it is shown in Appendix A that a sufficient number of 3D views is approximated by

$$M \geq \frac{\Delta\omega}{2\pi W_m} (2\pi r_m W_m + 5/2)^2, \quad (25)$$

where r_m is the maximum radius of the perturbation density, W_m is the maximum spatial frequency in the reconstruction, and $\Delta\omega$ is the spatial frequency of the deconvolved images. The expression in Eq.(25) can be derived from the 3D Projection-Slice Theorem (Eq.(12)) by consideration of the number of spherical harmonics in the function $\delta\tilde{\mu}_a^{35}$. Note that the relevant image resolution pertains to the *deconvolved* image V (in Eq.(20)), which is expected to have much higher spatial frequencies (hence greater $\Delta\omega$) than the blurred, measured images. For example, assuming a $5.0mm$ tumor imaged to $2.0mm$ resolution with $\Delta\omega \approx W_m$, an estimate of 17 look directions is obtained from Eq.(25).

Another application of the tomographic formalism is in estimates of the optimum look directions determined by the 3D angle metric^{35,36}

$$\Theta(\theta) = \int d\vec{r}_d P_{\hat{\theta}} P_{\hat{\theta}}^\# [J \otimes D_{\hat{\theta}}^{-1} \otimes U_{1_t}](\hat{\theta}, \vec{r}_d) [J \otimes D_{\hat{\theta}}^{-1} \otimes U_{1_t}](\hat{\theta}, \vec{r}_d), \quad (26)$$

which is a measure of the contribution of the $\hat{\theta}$ -image to the overall reconstruction. The expression in Eq.(26) is the overlap of the attenuation function and the backprojection of the image at $\hat{\theta}$. By consideration of simple shapes, it has been shown that the optimum look directions are toward the sharper ends of an elongated object³⁷. The expression in Eq.(26), derived in Appendix B, assumes prior knowledge of the density function shape, so may be useful for re-imaging and processing to enhance an earlier reconstruction.

5. SIMULATIONS

In this section, we apply the 3D tomographic reconstruction algorithm to a simulated data set for demonstration purposes, and explore in a preliminary way some of the limits of its applicability. The simulations are suggested by the tissue parameters and geometry of the measurements of Ref.(19), where a single view was used to reconstruct a slice of tissue, and are reflective of *in-vitro* measurements of human tissue. Here we use twelve view directions to image a cube of tissue 5.3 cm on a side, with a reduced scattering coefficient $\mu'_s = 0.8\text{cm}^{-1}$ and an absorption coefficient μ_a of 0.02cm^{-1} to give an attenuation constant $\kappa_0 = 0.69\text{cm}^{-1}$. In this cube two absorptive perturbations are centered at (x, y, z) coordinates $(-0.2\text{cm}, -0.2\text{cm}, 0.0\text{cm})$ and $(0.2\text{cm}, 0.2\text{cm}, 0.0\text{cm})$, respectively. The perturbations are 3D gaussian spheres which have an intensity distribution of the form, $\exp(-\alpha(\vec{r} - \vec{r}_c)^2)$, where the coefficient α is set to 2cm^{-1} and \vec{r}_c is the coordinate of the perturbation center given above. This functional form was chosen to mimic a spreading distribution of contrast agent localized around an absorptive site. Sampling was done on a mm scale so that each voxel was 1 mm^3 . Figure 3 shows the distribution of the tissue perturbations on a slice through the $z = 0$ plane of the tissue. Figure 4 shows the twelve imaging directions used for the reconstruction. These vertices represent both illumination and detection plane directions. These directions were chosen based on previous studies to determine optimal integration for functions on a sphere.³⁹

The first step in the simulation is to create the “measured” image for each view direction. For the demonstration purposes, this was done by projecting the tissue inhomogeneities into the twelve imaging plane directions and convolving these images with the “convolution filter”, \tilde{D}_θ , from Eq.(13), to blur the projection. This low-pass filtering process approximately reproduces the blurring which would occur from tissue propagation, and we observe that we do in fact obtain images which

correspond roughly to overlapping point sources at the appropriate depth. Figure 5 shows the relative intensity on the detector plane for one of the projection angles, which we take as an approximation to the “measured” transillumination difference image, U_{1t} , of Eq.(1). The other direction angles look similar and show a single wide maximum which does not separate the perturbations. This illustrates the inherent difficulty of imaging in highly scattering media. These projections were performed with an algorithm first described to process computed tomography data.⁴⁰

Figure 6 shows the reconstruction of tissue inhomogeneities using the projected difference images from all twelve directions. Here we used a conventional backprojection reconstruction algorithm, meaning we used Eq.(24), *but with no deconvolution filter*, so that $\tilde{D}_\theta^{-1}=1$. The two perturbations are not resolved, as we would expect from the image plane result, and we obtain a blurred version of the original inhomogeneities. We note that in addition to the conventional “mag-f” filter, J , of Eq.(23), we used a gaussian taper filter with a full width at half maximum of $1.0mm^{-1}$ to mitigate ringing caused by the sharp cut-off of the mag-f filter.⁴¹ We also note that some of the reconstruction has negative intensity. This results from application of the mag-f filter and is a known artifact of these kind of CT reconstructions. Figure 7 shows a similar reconstruction, in which depth estimates have been done at each beam direction to construct the deconvolution filter, D_θ^{-1} , of Eq.(24). These filters were then used in Eq.(24) to implement the full reconstruction algorithm including deconvolution. For these calculations the width of the taper filter was decreased, dampening the highest frequencies of the deconvolution filter and computations were done in double precision to better condition the numerical filtering process. In contrast to the reconstruction without the filter, this reconstruction clearly distinguishes the two perturbations, with intensities close to the original tissue of Fig. 3.

Actual measurements will of course have an amount of noise, which will be manifest in the projection plane difference images. This noise may come from the measurement process, or it may result from a delocalization of the contrast agent through the tissue. The noise is particularly troublesome for the reconstruction algorithm described here, since the deconvolution filter will accentuate high frequencies to a great degree, and therefore the effective signal-to-noise ratio of the reconstruction may become very low. To address these concerns in a preliminary way, we have performed the same reconstruction described above and have added noise to the tissue space before projecting to the image plane to create the “measured” images at each view. We added to each voxel in the tissue space random noise centered at 10^{-3} and with a similar spread relative to the maximum of the two “target” gaussian spheres. The resulting reconstruction is shown in Fig. 8. The two perturbations are still distinguishable, but the surrounding background tissue intensities show oscillations almost to the same level as the spheres making the effective signal-to-noise ratio quite low. The deconvolution algorithm is clearly sensitive to noise. On the other hand, use of more beams in the reconstruction, or more effective tapers which retain the high frequencies while keeping the noise low, may mitigate these problems. We are encouraged that recent experimental work using *ad-hoc* deconvolution filtering and backprojection appears to create useful reconstructions.⁴² We have also explored the sensitivity of the method to errors in the depth estimate. This has not been a large source of error in the previous examples, but in practice such errors will occur. Figure 9 shows the reconstruction with noise and the deconvolution filter as in Fig. 8, with the addition of a random error in the depth for the filter in each beam direction of 20% standard deviation of the known depth centered around the estimated depth. The results are similar to Fig. 8, except there is less contrast in the tissue perturbations over the background. This is because the backprojections have an error due to imprecise deconvolution, in addition to the noise. For other situations, where the

inhomogeneities are distributed throughout the tissue, a single depth estimate will not suffice, and a series of reconstructions must be performed, one for each “absorption center”.

6. CONCLUSIONS

In this paper a unified algorithm for 3D DPDW imaging of absorptive perturbations in tissue with multiple transilluminated 2D views was derived. This algorithm is a generalization of previous work¹⁹ which uses a single view, and extends tomographic reconstruction algorithms based on the Projection-Slice Theorem in a formal way to include scattering media. An important aspect of this algorithm is the use of a deconvolution filter which compensates for the blurring from photon scattering. To construct the filter each look direction requires a depth estimate based on the width of the image plane response. The point source solution corresponding to the estimated depth is deconvolved from the image to obtain the x-ray transform of the perturbing attenuation function. The inversion of the processed images then requires filtering and backprojection.

The algorithm was demonstrated with data simulating the absorption of a contrast agent in human tissue. The use of a contrast agent is expected to suppress tissue inhomogeneities. It was found that the deconvolution filter was important to achieve good resolution. However, the deconvolution filter, which accentuates high frequencies, was shown to be sensitive to noise and the estimated depths of the tumor absorption. This type of processing will require careful treatment in practice, but we note that even for a measurement using a single view an effective tomographic reconstruction can be achieved.¹⁹ As noted by Schotland,⁷ perturbative approaches to the reconstruction problem are “subject to certain limitations” including the assumption that the reference medium is uniformly absorbing and scattering which appears not to be the case for biological tissues. Nevertheless, because backprojection of the transilluminated images are likely to

give a reasonable and computationally inexpensive first-order result, the present algorithm could be used as a starting point for an iterative approach to the inverse problem.

APPENDIX A: IMAGE NUMBER CONDITIONS

The Projection-Slice Theorem for the 3D x-ray transform relates the 2D Fourier transform of a projected image at angle $\hat{\theta}$ to a slice through the 3D Fourier transform of the reconstructed object²⁰. For the case of NIR imaging of an absorbing perturbation, the relationship in Eq.(12) relates the projected image to the absorption function convolved with the photon point spread function. The sampling geometry implied by the Projection-Slice Theorem is shown in Fig. A1, in which Fourier space samples on a slice through the origin are obtained from the Fourier transform of the projected image.

Generalizing the derivation of the ‘‘Bow Tie’’ condition in Ref.(38) for electron microscopy, we expand the absorption function $\delta\mu_a(\vec{r})$ and its Fourier transform in spherical harmonics. (It is assumed that the point spread function has been deconvolved in the following analysis.) The result is given by

$$\delta\mu_a(r, \theta, \phi) = \sum_{l=0}^{\infty} \sum_{m=-l}^l g_{lm}(r) Y_{lm}(\theta, \phi), \quad (\text{A1})$$

and

$$\delta\tilde{\mu}_a(W, \Theta, \Phi) = \sum_{l=0}^{\infty} \sum_{m=-l}^l G_{lm}(W) Y_{lm}(\Theta, \Phi), \quad (\text{A2})$$

where W is the magnitude of the 3D frequency vector $W\hat{\Theta}$. From the Funk-Henke Theorem for spherical harmonics $\{Y_{lm}\}$ ²⁰,

$$\int_{S^2} \exp(i\sigma\hat{\theta} \cdot \hat{\omega}) Y_{lm}(\hat{\omega}) d\hat{\omega} = (2\pi)^{3/2} i^l \frac{J_{l+1/2}(\sigma)}{\sqrt{\sigma}} Y_{lm}(\hat{\theta}), \quad (\text{A3})$$

where $\hat{\theta}$ denotes the unit vector $\hat{\theta} = (\theta, \phi)$ in S^2 (the unit sphere). The expression for the Fourier transform in spherical coordinates is

$$\delta\tilde{\mu}_a(W\hat{\Theta}) = \int \exp(i2\pi W\hat{\theta} \cdot \hat{\Theta}) \delta\mu_a(r\hat{\theta}) r^2 dr d\hat{\theta}. \quad (\text{A4})$$

We have by substitution of Eqs.(A1) and (A2),

$$G_{lm}(W) = \frac{(2\pi)^l i^l}{\sqrt{W}} \int r^{3/2} J_{(l+1/2)}(2\pi r W) g_{lm}(r) dr. \quad (\text{A5})$$

In Eqs.(A3) and (A5) J_n is the n^{th} order Bessel function.

From Eq.(12) and the geometry in Fig. A1, the deconvolved image $V(\hat{\theta}, \bar{y})$ at angle $\hat{\theta} \in S^2$ is related to the Fourier transform of the perturbation $\delta\mu_a$ by

$$\delta\tilde{\mu}_a(\bar{\eta}) = \tilde{V}(\hat{\theta}, \bar{\eta}); \bar{\eta} \in \Theta^\perp. \quad (\text{A6})$$

We are interested in the determination of the function $\delta\tilde{\mu}_a(\bar{\eta}), \bar{\eta} \in \Theta^\perp$, from the finite sampling of views $V(\hat{\theta}, \bar{y})$. From Eq.(A6), the image at angle $\hat{\Theta}_j, j=1, \dots, M$ determines frequency space samples of $\delta\tilde{\mu}_a(\bar{\eta})$ evaluated at $\bar{\eta} \in \Theta_j^\perp$. More specifically, substitution of $\bar{\eta} = W\hat{\Theta}_{jk}, \hat{\Theta}_{jk} \in \Theta_j^\perp, k=1, \dots, N_j$, into Eq.(A6) yields

$$\delta\tilde{\mu}_a(W\hat{\Theta}_{jk}) = \tilde{V}(\hat{\Theta}_j, W\hat{\Theta}_{jk}). \quad (\text{A7})$$

The geometry suggested by Eq.(A7) is shown in Fig. A1 in which samples on an annulus of radius W , from the beam oriented at angle $\hat{\Theta}_j$, are proportional to the corresponding frequency space samples of $\delta\tilde{\mu}_a(\vec{\eta})$.

The set $\{G_{lm}(W)\}$ completely determines the reconstructed function $\delta\tilde{\mu}_a(\vec{\eta})$ at a radial spatial frequency of W . Hence, the condition for reconstruction of $\delta\tilde{\mu}_a$ is the inversion of the matrix equation ($j = 1, \dots, M; k = 1, \dots, N_j$) for $\{G_{lm}(W)\}$ given by

$$\delta\tilde{\mu}_a(W\hat{\Theta}_{jk}) = \sum_{lm} G_{lm}(W)Y_{lm}(\hat{\Theta}_{jk}). \quad (\text{A8})$$

Defining the matrix $Y_{(jk)(lm)} \equiv Y_{lm}(\hat{\Theta}_{jk})$ we obtain

$$(Y \bullet (WG))_{(jk)} = W \sum_{lm} Y_{(jk)(lm)} G_{lm} = \tilde{V}(\hat{\Theta}_j, W\hat{\Theta}_{jk}). \quad (\text{A9})$$

Equation (A9) represents N_j equations (the number of samples in the plane Θ_j^\perp) among the unknowns $\{G_{lm}(W)\}$. Assuming a maximum value l of L in the expansion of Eq.(A2), the corresponding number of unknowns is $\sum_{l=0}^L (2l+1) = (L+1)^2$, which results in a consistency bound (number of equations \geq number of unknowns) given by

$$\sum_{j=1}^M N_j \geq (L+1)^2. \quad (\text{A10})$$

The number of samples obtained from each image for the reconstruction of $\delta\tilde{\mu}_a$ at frequency W is determined by the 2D Fourier transform of the image on the annulus of radius W . A resolution

length of $\Delta\omega$ in frequency on the image suggests a number of samples $N_j(W) = 2\pi W / \Delta\omega$.

Substitution into Eq.(A10) results in an image number threshold given by

$$M \geq \frac{\Delta\omega}{2\pi W} (L + 1)^2. \quad (\text{A11})$$

A sufficient (maximum) value for L can be estimated by assuming a maximum extent for the perturbation r_{\max} with the property $g_{lm}(r) = 0$ for $r \geq r_{\max}$ in Eq.(A1). Therefore, at a spatial frequency of W , a bound $2\pi r_{\max} W$ exists for the Bessel function argument in Eq.(A5). From the Debye approximation³⁸, $J_n(x) \cong 0$ for $n \geq (x + 2)$, substituted into Eq.(A5), we have $G_{lm}(W) \cong 0$ for $l \geq L \equiv (2\pi r_{\max} W + 3/2)$. Therefore, from Eq.(A11) a sufficient number of beams for reconstruction at frequency W is given by

$$M \geq \frac{\Delta\omega}{2\pi W} (2\pi r_{\max} W + 5/2)^2. \quad (\text{A12})$$

In the limit $2\pi r_{\max} W \gg 1$, Eq.(A12) is written

$$M \geq (r_{\max} \Delta\omega) 2\pi r_{\max} W_{\max}, \quad (\text{A13})$$

where W_{\max} is the maximum spatial frequency in the reconstructed function.

It is interesting to contrast the image number criterion for 2D and 3D cases. Two-dimensional reconstruction results in a bound

$$M \geq (2\pi r_{\max} W_{\max} + 5/2), \quad (\text{A14})$$

which is known as the ‘‘Bow Tie’’ condition in CT²⁰ and electron microscopy³⁸. The 2D inversion bound differs from the 3D bound because only one sample is obtained in frequency space for each

annulus. Therefore, the factor $r_{\max} \Delta\omega$, dependent on the *image* frequency space resolution, does not appear in the 2D bound. Note that the matrix inversion, although never actually computed, is more complex in the cylindrical case due to a required evaluation at each (W, Z) coordinate, rather than each radial spatial frequency W alone.

APPENDIX B: IMAGE ORIENTATION CONDITIONS

The reconstruction of the perturbation function $\delta\mu_a(\vec{r})$ from a discrete set of views, embodied as the matrix inversion in Eq.(A9), suggests that the generalized inverse of $Y_{(jk)(lm)}$ must be well-defined. This corresponds to the condition that the matrix

$$(Y^{*T}Y)_{(lm)(lm)} = \sum_{j=1}^M \sum_{k=1}^{N_j} Y_{(lm)(\hat{\Theta}_{jk})}^* Y_{(lm)(\hat{\Theta}_{jk})} \quad (\text{B1})$$

is non-singular. Therefore, the eigenvalues of $(Y^{*T}Y)$ in Eq.(B1) define a selection criterion at each frequency W for the set of view angles $\{\hat{\Theta}_j, j = 1, \dots, M\}$. For example, if the samples on the frequency space annulus in Fig. A1 are not independent, the inversion could require more views than suggested in Eq.(A11).

An additional selection criterion, which ranks individual views, is based on the metrics in the tissue and projection Hilbert spaces. The direct inner products in tissue and projection spaces between two perturbation functions f, g and images $\underline{f}, \underline{g}$ are defined by

$$[f, g] = \int_{R^2} f(\vec{x})g(\vec{x})d\vec{x}, \quad (\text{B2})$$

and

$$\langle \underline{f}, \underline{g} \rangle = \int_{R^2} \underline{f}(\hat{\theta}, \bar{y}) \underline{g}(\hat{\theta}, \bar{y}) d\bar{y}, \quad (\text{B3})$$

respectively²⁰. The dual x-ray transform is the metric space dual of the x-ray transform relative to the direct metrics. The duality relationship is expressed in the equation

$$[f, P^\# \underline{g}] = \langle Pf, \underline{g} \rangle, \quad (\text{B4})$$

where f and \underline{g} are functions in tissue and image spaces, respectively. Assuming a continuous profile function $\underline{f}(\hat{\theta}, \bar{y}), \bar{y} \in \theta^\perp$, define the sampled profile function \underline{f}_s by

$$\underline{f}_s(\hat{\theta}, \bar{y}) = \sum_{j=1}^M \delta(\hat{\theta} - \hat{\theta}_j) \underline{f}(\hat{\theta}_j, \bar{y}). \quad (\text{B5})$$

We are interested in maximizing the direct inner product between the perturbation functions corresponding to continuous and sampled views. Substitution of Eq.(21) into the direct inner product, and application of Eq.(B4), yields

$$[\delta\mu_a, \delta\mu_{a_s}] = \langle PP^\# [J \otimes V], (J \otimes V)_s \rangle. \quad (\text{B6})$$

Equation (B6) corresponds to an image space metric indicating that the contribution of views to the reconstruction of $\delta\mu_a$ are ranked in angle by the function

$$\Theta(\theta) = \int (P_\theta P_\theta^\# [J \otimes V](\hat{\theta}, \bar{y})) (J \otimes V(\hat{\theta}, \bar{y})) d\bar{y}, \quad (\text{B7})$$

which is derivable from the deconvolved images $\{V(\hat{\theta}, \bar{y})\}$.

REFERENCES

5. S.R. Deans, *The Radon Transform and some of its Applications*, (John Wiley and Sons, New York, 1983).

6. S. Webb, *The Physics of Three-dimensional Radiation Therapy, Conformal Radiotherapy, Radiosurgery, and Treatment Planning*, (Institute of Physics Publishing, Bristol, 1993).
7. O’Leary, M.A., Boas, D., Chance, B., and Yodh, A., *Phys. Rev. A.*, **69**, 2658-2661, (1992).
- A. Yodh and B. Chance, “Spectroscopy and Imaging with Diffusing Light,” *Physics Today*, March, 1995, 34-40, and references therein.
8. S.R. Arridge and J. C. Hebden, “Optical Imaging in Medicine: II. Modelling and Reconstruction,” *Phys. Med. Biol.*, **42**, 841-853, (1997).
9. I.W. Kwee, Y. Tanikawa, S. Proskurin, S.R. Arridge, D.T. Delphy, and Y. Yamada, “Performance of a Null-space Image Reconstruction Algorithm,” in *Optical Tomography and Spectroscopy of Tissue: Theory, Instrumentation, Model, and Human Studies II*, B. Chance and R. R. Alfano, eds., *Proc. SPIE*, **2979**, 185-196, (1997).
10. J.C. Schotland, “Continuous-wave Diffusion Imaging,” *J. Opt. Soc. Am. A*, **14**, 275-279, (1997).
11. Y. Yao, Y. Pei, Y. Wang, and R.L. Barbour, “A Born type Iterative Method for Imaging of Heterogeneous Scattering Media and its Application to Simulated Breast Tissue,” in *Optical Tomography and Spectroscopy of Tissue: Theory, Instrumentation, Model, and Human Studies II*, B. Chance and R. R. Alfano, eds., *Proc. SPIE*, **2979**, 232-240, (1997).
12. M.V. Klivanov, T.R. Lucas, and R.M. Frank, “New Imaging Algorithm in Diffusion Tomography,” in *Optical Tomography and Spectroscopy of Tissue: Theory, Instrumentation, Model, and Human Studies II*, B. Chance and R. R. Alfano, eds., *Proc. SPIE*, **2979**, 272-283, (1997).
13. See, for example, B. Chance and R. Alfano, eds., *Proceedings of Optical Tomography and Spectroscopy of Tissue: Theory, Instrumentation, Model, and Human Studies II, Volume 2979*, (SPIE Press, Bellingham, WA, 1997).

14. J.T. Bruulsema, J.E. Hayward, T.J. Farrell, M. Essenpreis, and M.S. Patterson, "Optical Properties of Phantoms and Tissue Measured in vivo from 0.9 – 1.3 μ m using Spatially Resolved Diffuse Reflectance," in *Optical Tomography and Spectroscopy of Tissue: Theory, Instrumentation, Model, and Human Studies II*, B. Chance and R. R. Alfano, eds., Proc. SPIE, **2979**, 325-334, (1997).
15. V.G. Peters, D.R. Wyman, M.S. Patterson, and G.L. Frank, "Optical Properties of Normal and Diseased Human Breast Tissues in the Visible and Near Infrared," *Phys. Med. Biol.*, **35**, 1317-1334, (1990).
16. W.-F. Cheong, S.A. Prahl, A.J. Welch, "A Review of Optical Properties of Biological Tissues," *IEEE J. Quantum Electronics*, **26**, 2166-2185, (1990).
17. R.J. Grable, D.P. Rohler, and K. Sastry, "Optical Tomography Breast Imaging," in *Optical Tomography and Spectroscopy of Tissue: Theory, Instrumentation, Model, and Human Studies II*, B. Chance and R. R. Alfano, eds., Proc. SPIE, **2979**, 197-210, (1997).
18. S.A. Walker, A.E. Cerussi, and E. Gratton, "Back-projection Image Reconstruction using Photon Density Waves in Tissues," in *Optical Tomography: Photon Migration and Spectroscopy of Tissue and Model Media: Theory, Human Studies and Instrumentation*, B. Chance ed., Proc. SPIE, **2389**, 350-357, (1995).
19. S.B. Colak, H. Schomberg, G.W. 't Hooft, and M.B. van der Mark, "Optical BackProjection Tomography in Heterogeneous Diffusive Media," in R.R. Alfano and J.G. Fujimoto, eds., *OSA TOPS in Advances in Optical Imaging and Photon Migration*, **2**, 282-289,(1996).
20. S.B. Colak, D.G. Papaioannou, G.W. 't Hooft, and M.B. van der Mark, "Optical Image Reconstruction with Deconvolution in Light Diffusing Media," in *Photon Migration in Tissues*, B. Chance, D. T. Delpy, and G. J. Mueller, eds., Proc. SPIE, **2626**, 306-315, (1995).

21. A.J. Devaney, "Reconstructive Tomography with Diffracting Wavefields," *Inverse Problems*, **2**, 161-183, (1986).
22. X.D. Li, T. Durduran, A.G. Yodh, B. Chance, and D.N. Pattanayak, "Diffraction Tomography for Biochemical Imaging with Diffuse-photon Density Waves," *Optics Letters*, **22**, 573-575, (1997).
23. F. Natterer, *The Mathematics of Computerized Tomography*, (John Wiley and Sons, New York, 1986).
24. S.C. Feng, F.-A. Zeng, and B. Chance, "Analytical Perturbation Theory of Photon Migration in the Presence of a Single Absorbing or Scattering Defect Sphere," in *Optical Tomography: Photon Migration and Spectroscopy of Tissue and Model Media: Theory, Human Studies and Instrumentation*, B. Chance ed. Proc. SPIE, **2389**, 54-63, (1995).
25. D.A. Boas, M.A. O'Leary, B. Chance, and A.G. Yodh, "Scattering of Diffuse Photon Density Waves by Spherical Inhomogeneities within Turbid Media: Analytic Solution and Applications," *Proc. Natl. Acad. Sci.*, **91**, 4887-4891, (1994).
26. S. Fantini, S.A. Walker, M.A. Franceschini, M. Kaschke, P.M. Schlag, and K.T. Moesta, "Assessment of the Size, Position, and Optical Properties of Breast Tumors *in vivo* by Noninvasive Optical Methods," *Applied Optics*, **37**, 1982-1989, (1998).
27. L.S. Heuser and F.N. Miller, "Differential Macromolecular Leakage from the Vasculature of Tumors," *Cancer*, **57**, 461-464, (1986).
28. X. Li, B. Beauvoit, R. White, S. Nioka, B. Chance, and A. Yodh, "Tumor Localization using Fluorescence of Indocyanine Green (ICG) in Rat Models," in *Optical Tomography: Photon Migration and Spectroscopy of Tissue and Model Media: Theory, Human Studies and Instrumentation*, B. Chance ed. Proc. SPIE, **2389**, 789-797, (1995).

29. M.M. Haglund, D.W. Hochman, A.M. Spence, and M.S. Berger, "Enhanced Optical Imaging of Rat Gliomas and Tumor Margins, *Neurosurgery*, **35**, 930-940, (1994).
30. N. Weidner, J.P. Semple, W.R. Welch, and J. Folkman, "Tumor Angiogenesis and Metastasis-Correlation in Invasive Breast Carcinoma," *New Eng. J. Med.*, **324**, 1-7, (1991).
31. S.P. Gopinath, C.S. Robertson, R.G. Grossman, and B. Chance, "Near-infrared Spectroscopic Localization of Intracranial Hematomas," *J. Neurosurg.*, **79**, 43-47, (1993).
32. M. Braunstein, R.W. Chan, and R.Y. Levine, "Simulation of Dye-enhanced Near-IR Transillumination Imaging of Tumors," *Proceedings of the IEEE Engineering in Medicine and Biology 19th Annual International Conference*, p. 93, Oct. 30, 1997, IEEE New York, publishers.
33. M. Braunstein, R.W. Chan, and R.Y. Levine, "Dye-enhanced Multispectral Transillumination for Breast Cancer Detection: Feasibility Measurements," *Proc. IEEE Engineering in Medicine and Biology 19th Annual International Conference*, p. 91, Oct. 30, 1997, IEEE, New York, publishers.
34. S. Zhou, M.A. O'Leary, S. Nioka, and B. Chance, "Breast Tumor Detection using Continuous Wave Light Source," in *Optical Tomography: Photon Migration and Spectroscopy of Tissue and Model Media: Theory, Human Studies and Instrumentation*, B. Chance ed. *Proc. SPIE*, **2389**, 809-817, (1995).
35. T. Carski, "Indocyanine Green: History, Chemistry, Pharmacology, Indications, Adverse Reactions, Investigation and Prognosis: An Investigative Brochure," Becton Dickinson and Company, Inc., Cockeysville, Maryland, March 17, 1995.
36. X. Wu, L. Stinger, and G.W. Faris, "Determination of Tissue Properties by Immersion in a Matched Scattering Fluid," in *Optical Tomography and Spectroscopy of Tissues: Theory*,

- Instrumentation, Model, and Human Tissues*, B. Chance and R. R. Alfano eds. Proc. SPIE, **2979**, 300-306, (1997).
37. A. Ishimaru, *Wave Propagation and Scattering in Random Media, Volume 1, Single Scattering and Transport Theory*, (Academic Press, New York, 1978), 175-185.
38. R.Y. Levine, E.A. Gregerson, and M.M. Urie, "The Application of the X-ray Transform to 3D Conformal Radiotherapy" in C. Borgers and F. Natterer, eds., *Computational Radiology and Imaging: Therapy and Diagnostics*, (Springer-Verlag, New York, 1999).
39. B.P. Medoff, "Image Reconstruction from Limited Data: Theory and Applications in Computerized Tomography," in H. Stark, ed., *Image Recovery: Theory and Application*, (Academic Press, New York, 1987).
40. M. Braunstein and R.Y. Levine, "Optimum Beam Configurations in Tomographic Intensity Modulated Radiation Therapy", submitted for publication, *Phys. Med. Biol.*, March, 1999.
41. Crowther, R.A., DeRosier, D.J., and Klug, A., "The Reconstruction of a Three-dimensional Structure from Projections and its Application to Electron Microscopy," *Proc. Roy. Soc. Lond. A.*, **317**, 319-340, (1970).
42. W. Neutsch, "Optimal Spherical Design and Numerical Integration on the Sphere", *J. of Comp. Phys.* **51**, 313-325 (1983).
43. R. L. Siddon, "Fast Calculation of the Exact Radiological Path for a Three-Dimensional CT Array", *Med. Phys.* **12**, 252-255 (1985).
44. G. T. Gullberg and T. F. Budinger, "The Use of Filtering Methods to Compensate for Constant Attenuation in Single-Photon Emission Computed Tomography", *IEEE Trans. Bio. Eng.* **BME-28**, 142-157 (1981).

45. R. J. Grable, D. P. Rohler, and S. Kla, in *Optical Tomography and Spectroscopy of Tissues: Theory, Instrumentation, Model, and Human Tissues*, B. Chance and R. R. Alfano eds. Proc. SPIE, **2979**, 197-210, (1997).

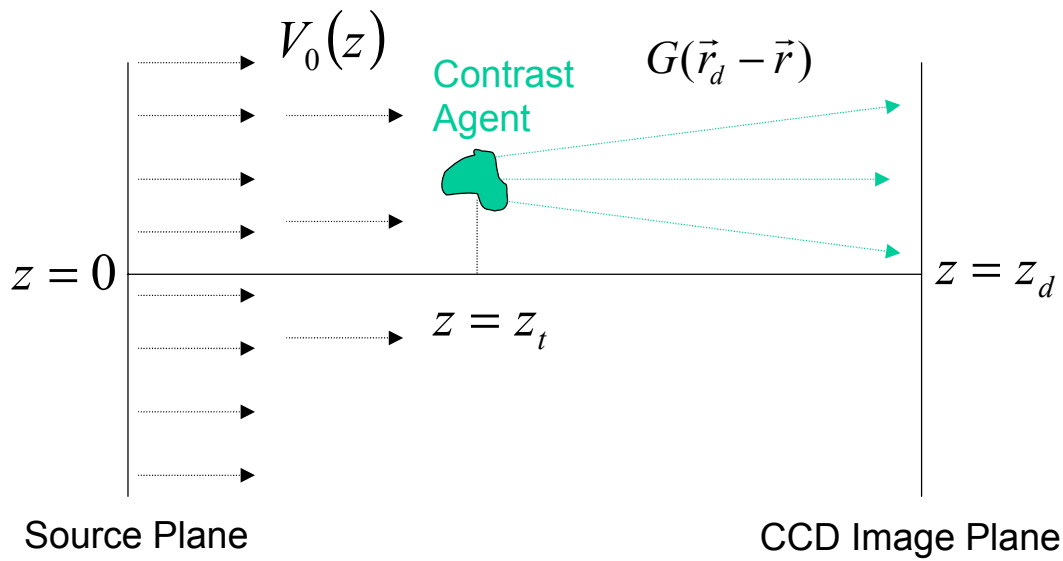


Figure 1. Sideview of tomographic DPDW measurement of contrast agent attenuation.

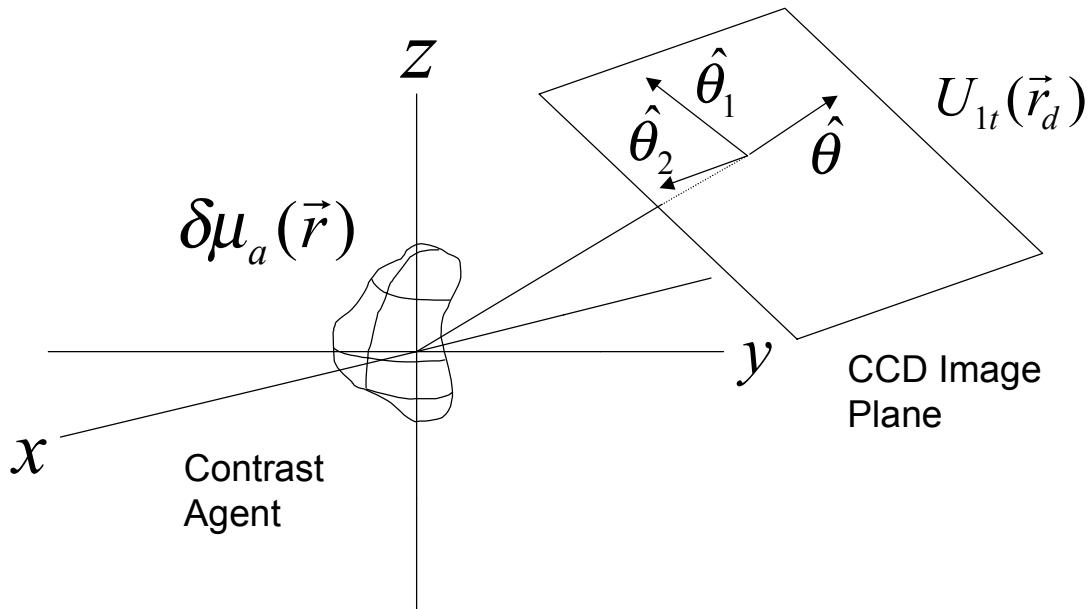


Figure 2. Geometry of multi-spectral 3D tomographic imaging of a contrast agent.

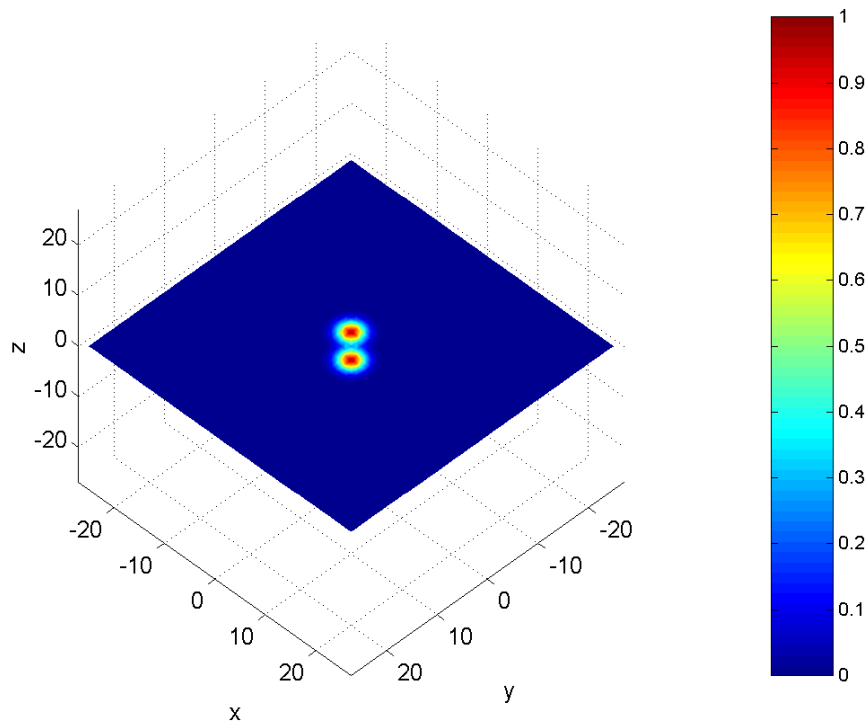


Figure 3. Distribution of tissue perturbation. A slice through the $z=0$ plane is shown. Axes are in units of mm and the intensity has been normalized to 1.0 at the maximum.

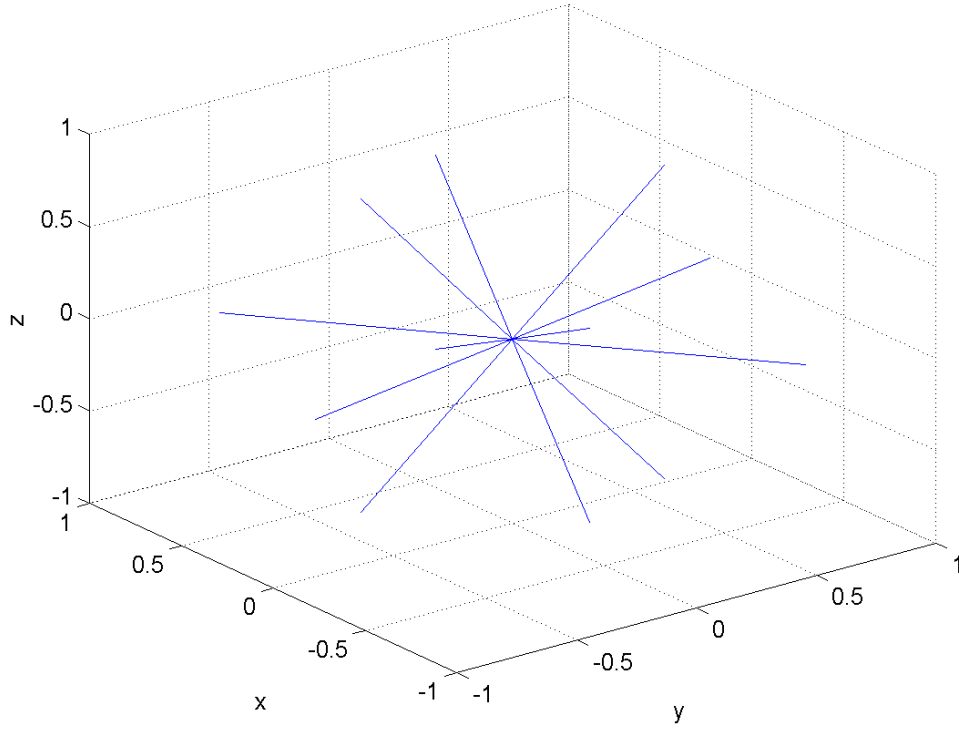


Figure 4. Imaging directions for 3D transillumination reconstruction. Units are relative.

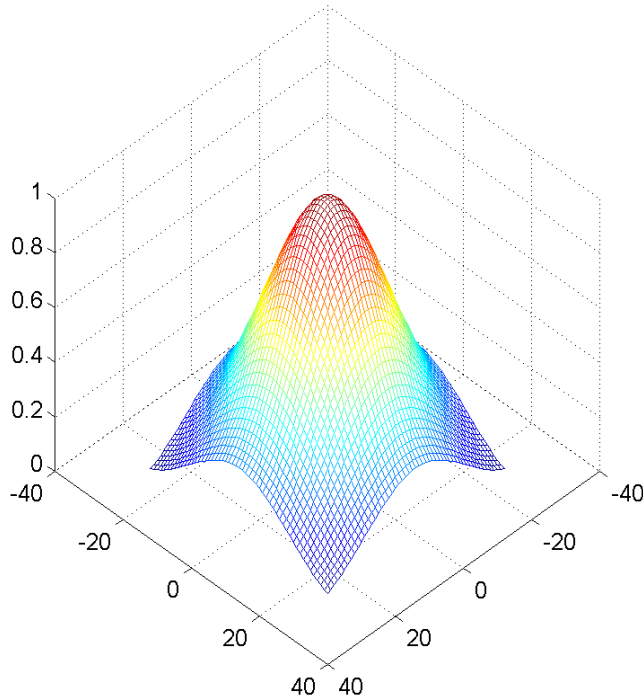


Figure 5. Relative intensity on the detector plane for one of the projection angles. The (x, y) points are in units of mm , and the z direction shows the relative intensity.

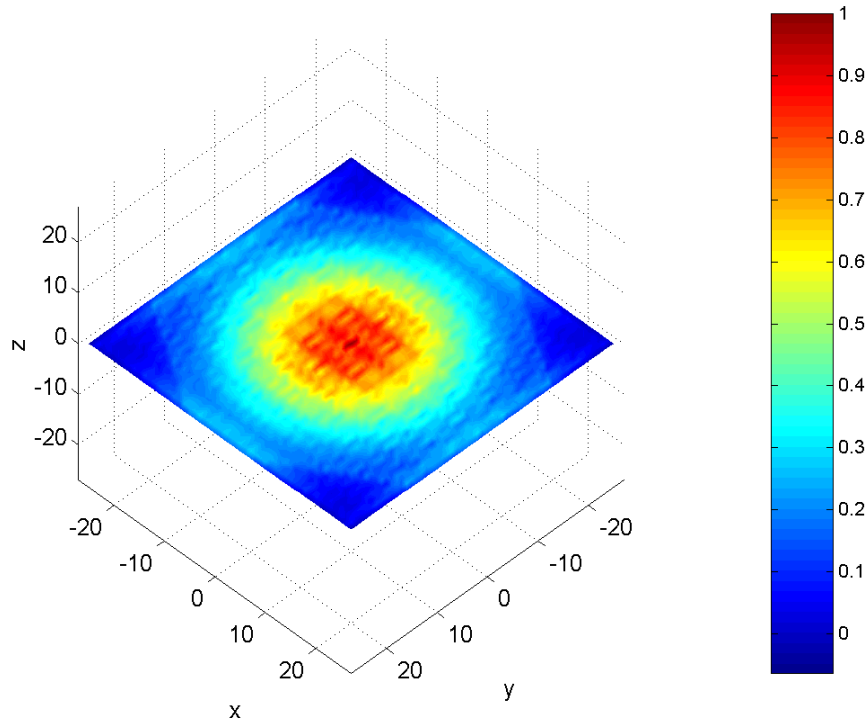


Figure 6. Reconstruction of tissue perturbations using all twelve views. A slice through the $z = 0$ plane is shown. Axes are in units of mm and the intensity has been normalized to 1.0 at the maximum. No deconvolution was performed.

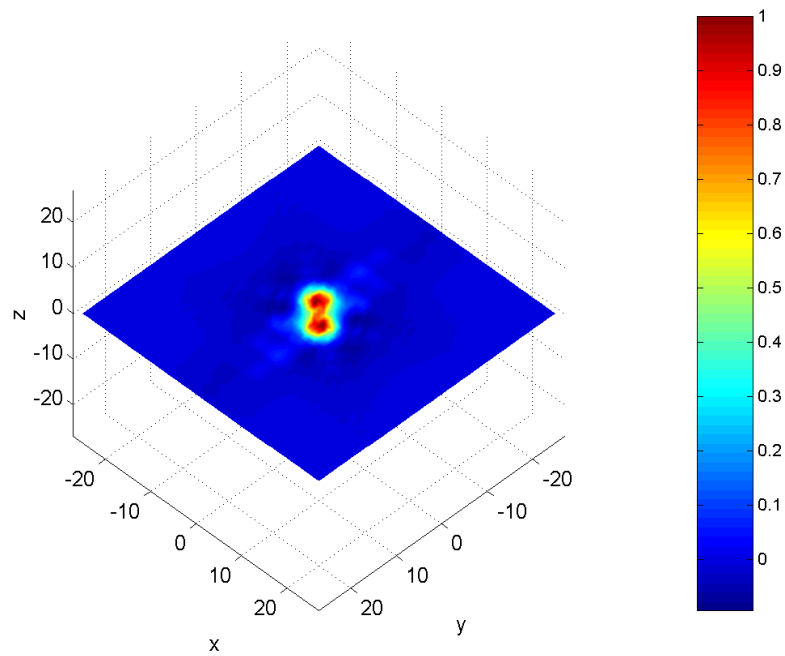


Figure 7. The same as Fig. 6 except deconvolution of the projected images was performed prior to backprojection.

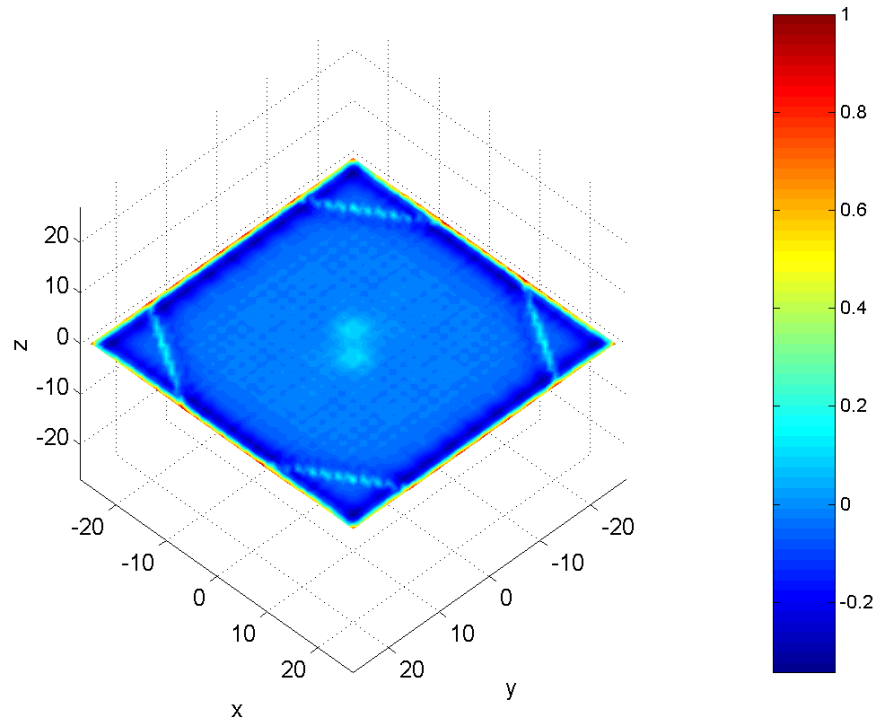


Figure 8. The same as Fig. 7 but noise has been added to the tissue volume to create the simulated images used for the reconstruction.

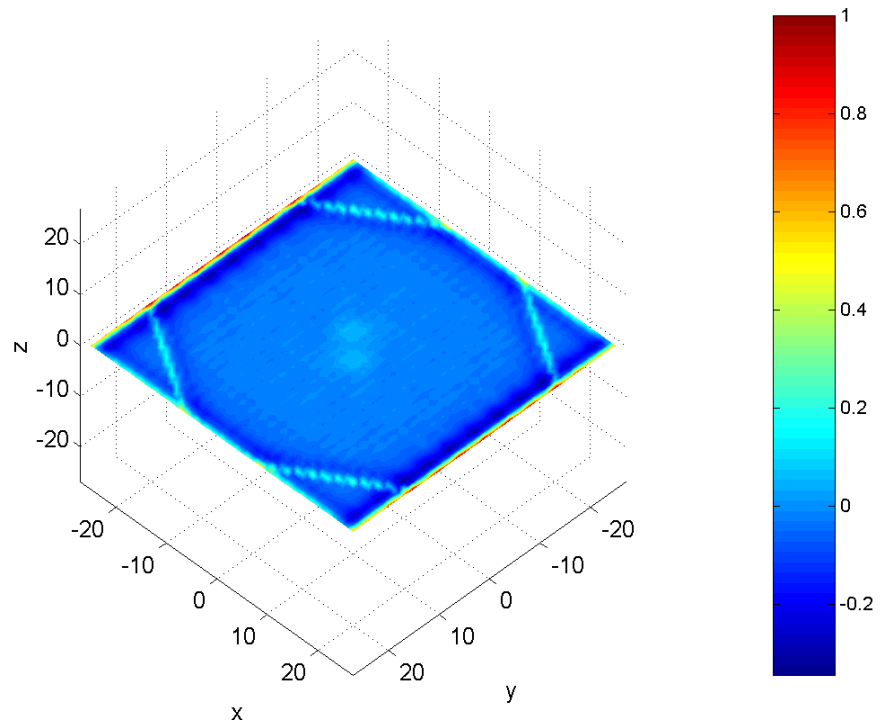


Figure 9. The same as Fig. 8, but with uncertainty in the depth estimation.

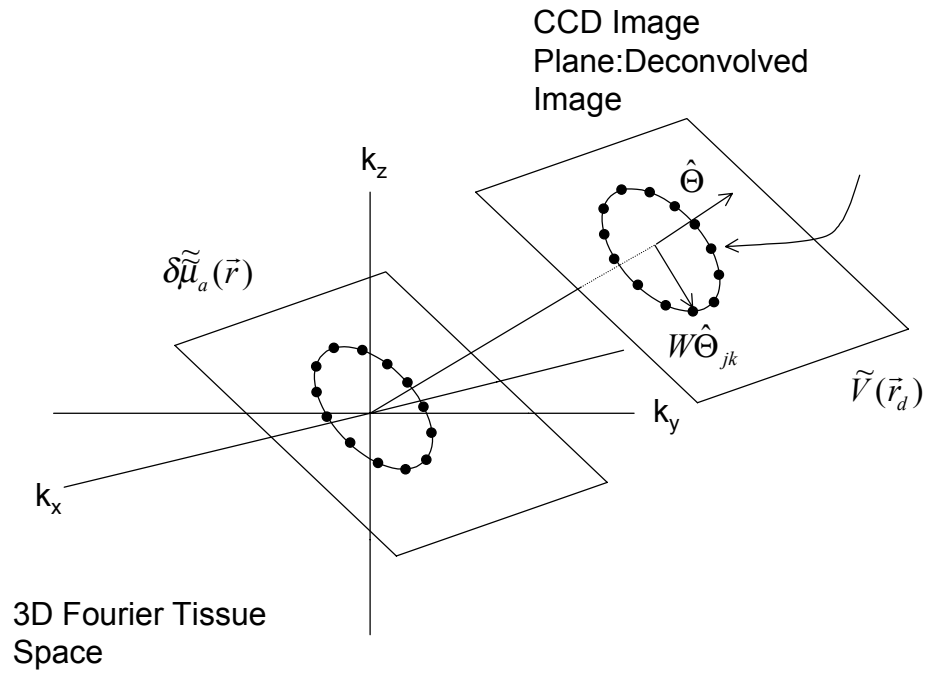


Figure A1. Geometry for determination of the number of views necessary for reconstruction to achieve a given resolution. It is assumed that the images have already been deconvolved, as discussed in the text.